Multivariate Shape Modeling and Its Application to Characterizing Abnormal Amygdala Shape in Autism

Moo K. Chung[a,b*], Keith J. Worsley[d], Brendon, M. Nacewicz[b], Kim M. Dalton[b], Richard J. Davidson[b,c]

[a]Department of Biostatistics and Medical Informatics
[b]Waisman Laboratory for Brain Imaging and Behavior
[c]Department of Psychology and Psychiatry
University of Wisconsin, Madison, WI 53706, USA

[d]Department of Statistics
University of Chicago, Chicago, IL 60637, USA

September 22, 2009

Abstract

Although there are many imaging studies on traditional ROI-based amygdala volumetry, there are very few studies on modeling amygdala shape variations. This paper present a first unified computational and statistical framework for modeling amygdala shape variations in a clinical population. The recently developed weighted spherical harmonic representation is used as to parameterize, to smooth out, and to normalize amygdala surfaces. The representation is subsequently used as an input for multivariate linear models accounting for age and brain size difference using `SurfStat` package that completely avoids the complexity of specifying design matrices. The methodology has been applied to detect abnormal local shape variations in 22 high functioning autistic subjects. We have localized significant shape difference in autism in the right amygdala. Further we have detected significant difference in interaction of shape and gaze fixation duration indicating localized abnormal association

*Corresponding address: Moo K. Chung, Waisman Center #437, 1500 Highland Ave. Madison, WI. 53705. telephone: 608-217-2452, email://mkhung@wisc.edu, http://www.stat.wisc.edu/∼mchung

of function and structure in autism.

Keywords: Amygdala, Spherical Harmonics, Fourier Analysis, Surface Flattening, General Linear Model, SurfStat

1. Introduction

Amygdala is an important brain substructure that has been implicated in abnormal functional impairment in autism (Dalton et al., 2005; Nacewicz et al., 2006; Rojas et al., 2000). Since the abnormal structure might be the cause of the functional impairment, there have been many studies on amygdala volumetry. However, previous amygdala volumetry results have been inconsistent. Aylward et al. (1999) and Pierce et al. (2001) reported that amygdala volume was significantly smaller in the autistic subjects while Howard et al. (2000) and Sparks et al. (2002) reported larger volume. Haznedar et al. (2000) and Nacewicz et al. (2006) found no volume difference. Schumann et al. (2004) reported that age dependent amygdala volume difference in autistic children and indicated that the age dependency to be the cause of discrepancy. All these previous studies traced the amygdalae manually and by counting the number of voxels within the region of interest (ROI), the total volume of the amygdala was estimated. The limitation of the traditional ROI-based volumetry is that it can not determine if the volume difference is diffuse over the whole ROI or localized within specific regions of the ROI (Chung et al., 2001). We present a novel computational and statistical framework that enables localized amygdala shape characterization and able to overcome the limitation of the ROI-based volumetry.

1.1 *Previous Shape Models*

Although there are extensive literature on local cortical shape analysis (Chung et al., 2005; Fischl and Dale, 2000; Joshi et al., 1997; Taylor and Worsley, 2008; Thompson and Toga, 1996; Lerch and Evans, 2005; Luders et al., 2006; Miller et al., 2000), there are almost no literature on amygdala shape analysis other than Qiu et al. (2008) mainly due to the difficulty of segmenting amgydala. On the other hand, there are extensive literature on shape modeling other subcortical structures using various techniques.

The medial representation (Pizer et al., 1999) has been successfully applied to various subcortical structures including the cross section of the corpus callosum (Joshi et al., 2002)

and hippocampus/amygdala complex (Styner et al., 2003), and ventricle and brain stem (Pizer et al., 1999). In the medial representation, the binary object is represented using the finite number of atoms and links that connect the atoms together to form a skeletal representation of the object. The medial representation is mainly used with the principal component type of analysis for shape classification and group comparison.

Unlike the medial representation, which is in a discrete form, there is a continuous parametric approach called the spherical harmonic representation (Gerig et al., 2001; Gu et al., 2004; Kelemen et al., 1999; Shen et al., 2004). The spherical harmonic representation has been mainly used as a data reduction technique for compressing global shape features into small number of coefficients. The main global geometric features are encoded in low degree coefficients while the noise will be in high degree spherical harmonics (Gu et al., 2004). The method has been used to model various subcortical structures such as ventricles (Gerig et al., 2001), hippocampi (Shen et al., 2004) and cortical surfaces (Chung et al., 2007).

The spherical harmonics have global support. So the spherical harmonic coefficients contain only the global shape features and it is not possible to directly obtain local shape information from the coefficients only. However, it is still possible to obtain local shape information by evaluating the representation at each fixed point, which gives the smoothed version of the coordinates of surfaces. In this fashion, the spherical harmonic representation can be viewed as mesh smoothing. Chung et al. (2007) have used the spherical harmonic representation in performing local shape analysis. Instead of using the global basis of spherical harmonics, there have been attempts of using the local wavelet basis for parameterizing cortical surfaces (Nain et al., 2007; Yu et al., 2007).

Other shape modeling approaches include distance transforms (Leventon et al., 2000) and deformation fields (Miller et al., 1997) obtained by warping individual substructures to a template. A distance transform is a function that for each point in the image is equal to the distance from that point to the boundary of the object (Golland et al., 2001). The distance map approach has been applied in classifying a collection of hippocampus (Golland et al., 2001). The deformation fields based approach has been somewhat popular and has been applied to modeling whole 3D brain volume (Ashburner et al., 1998; Chung et al., 2001; Gaser et al., 1999), cortical surfaces (Chung et al., 2003; Thompson et al., 2000), hippocampus (Joshi et al., 1997), cingulate gyrus (Csernansky et al., 2004).

1.2 *Available Computer Packages*

Over the years, various neuroimage processing and analysis packages have been developed. The SPM (`www.fil.ion.ucl.ac.uk/spm`) and AFNI (`afni.nimh.nih.gov`) software packages have been mainly designed for the whole brain volume based processing and univariate linear model type of analyses. Then the traditional statistical inference is used to test hypotheses about the parameters of the model parameters. The subsequent multiple comparisons problem is addressed using continuous random field theory. Although SPM and AFNI are probably two most widely used analysis tools, their analysis pipelines are based on a univariate general linear model and they do not have a routine for a multivariate analysis. Therefore, they do not have the subsequent routine for correcting multiple comparison corrections for the multivariate linear models as well.

Unlike SPM and AFNI, which are 3D whole brain volume based tools, there are few cortical surface based tools such as the surface mapper (SUMA) (Saad et al., 2004) and FreeSurfer (`surfer.nmr.mgh.harvard.edu`). Also the spherical harmonic modeling tool SPHARM-PDM (`www.ia.unc.edu/dev/download/shapeAnalysis`) is also available. However, these surface tools mainly do image processing and mesh representation and do not have the support for multivariate analysis. For instance, SPHARM-PDM only supports for doing univariate analysis by the projection of distance to the mean surface to its surface normal.

For multivariate linear modeling, one has to actually use statistical packages such as Splus (`www.insightful.com`), R (`www.r-project.org`) and SAS (`www.sas.com`). These statistical packages do not interface with imaging data easily so the additional processing step is needed to read and write imaging data within the software. Further these tools do not have the random field based multiple comparison correction procedures so the users are likely export analyzed statistics map to SPM or fMRISTAT (`www.math.mcgill.ca/keith/fmristat`) increasing the burden of additional processing steps.

1.3 *Our Contributions*

In this paper, we use the recently developed *weighted spherical harmonic representation* (Chung et al., 2007) for parameterization, surface smoothing and surface registration in a unified Hilbert space framework. Chung et al. (2007) presented the underlying mathematical theory and a new iterative algorithm for estimating the coefficients of the representation for

extremely large meshes such as cortical surfaces. Here we apply the method to real autism surface data in a truly multivariate fashion for the first time.

Our approach differs from the traditional spherical harmonic representation. Although the truncation of the series expansion in the traditional representation can be viewed as a form of smoothing, there is no direct equivalence to the *full width at half maximum* (FWHM) usually associated with kernel smoothing. So it is difficult to relate the unit of FWHM widely used in brain imaging to the spherical harmonic representation. On the other hand, our new representation can easily relate to FWHM of smoothing kernel so we have the clear sense of how much smoothing we are performing before hand.

The traditional series expansion suffers from the Gibbs phenomenon (ringing artifacts) (Gelb, 1997) that usually happens in representing rapidly changing or discontinuous data with smooth periodic basis. Our new representation can substantially reduce the amount of Gibbs phenomenon by weighting the coefficients of the spherical harmonic expansion. The weighting has the effect of actually performing heat kernel smoothing, and thus reducing the ringing artifacts. We demonstrate the better performance of our new representation in the both real and simulated data for the first time.

Since the proposed representation technique requires a smooth map from amygdala surfaces to a sphere, we have developed a new and very fast surface flattening technique based on the propagation of heat diffusion. By tracing the integral curve of heat gradient from a heat source (amygdala) to a heat sink (sphere), we can obtain the flattening map. Since solving an isotropic heat equation in a 3D image volume is fairly straightforward, our proposed method offers a much simpler numerical implementation than available surface flattening techniques such as conformal mappings (Angenent et al., 1999; Gu et al., 2004; Hurdal and Stephenson, 2004) quasi-isometric mappings (Timsari and Leahy, 2000) and area preserving mappings (Brechbuhler et al., 1995). The established spherical mapping is used to parameterize an amygdala surface using two angles associated with the unit sphere. The angles serve as coordinates for representing amygdala surfaces using the weighted linear combination of spherical harmonics. The streamlined tools containing the weighted spherical harmonic representation and the flattening algorithm can be found in `www.stat.wisc.edu/~mchung/research/amygdala`. It should be pointed out that our representation and paramterization techniques are general enough to be applied to various

brain structures such as hippocampus, caudate and cortical surfaces that are topologically equivalent to a sphere.

Based on the weighted spherical harmonic representation of amygdalae, various multivariate tests were performed to detect the group difference between autistic and control subjects. Most of multivariate shape models on coordinates and deformation vector fields have mainly used the Hotelling's T-sqaure as a test statistic (Cao and Worsley, 1999; Chung et al., 2001; Collins et al., 1998; Gaser et al., 1999; Joshi et al., 1997; Thompson et al., 1997). The Hotelling's T-sqaure statistic tests for the equality of vector means between two groups without the additional covariates such as gender, brain size, age and other covariates. Since the size of amygdala is dependent on brain size and possibly on age as well, there is a definite need for a model that able to include these covariates explicitly. The proposed multivariate linear model does exactly this by generalizing the Hotelling's T-square framework.

In order to simplify the computational burden of setting up the proposed multivariate linear models, we have developed the SurfStat package (`www.stat.uchicago.edu/~worsley/surfstat`) (Worsley et al., 2009) that offers a unified statistical analysis platform for various 2D surface mesh and 3D image volume data. The novelty of SurfStat package is that there is no need to specify design matrices that tend to baffle researchers not familiar with contrasts and design matrices. SurfStat supersedes fMRISTAT, and contains all the statistical and multiple comparison correction routines.

2. Methods

2.1 *Surface Parameterization*

Once the binary segmentation $\mathcal{M}_a$ of an object is obtained either manually or automatically, the marching cubes algorithm (Lorensen and Cline, 1987) was applied to obtain a triangle surface mesh $\partial\mathcal{M}_a$. The weighted spherical harmonic representation requires a smooth mapping from the surface mesh to a unit sphere S^2 to establish a coordinate system. We have developed a new surface flattening algorithm based on heat diffusion.

We start with putting a larger sphere $\mathcal{M}_s$ that encloses the binary object $\mathcal{M}_a$. Figure 2 shows an illustration with the binary segmentation of amygdala. The center of the sphere $\mathcal{M}_s$ is taken as the average of the mesh coordinates of $\partial\mathcal{M}_a$, which forms the surface mass

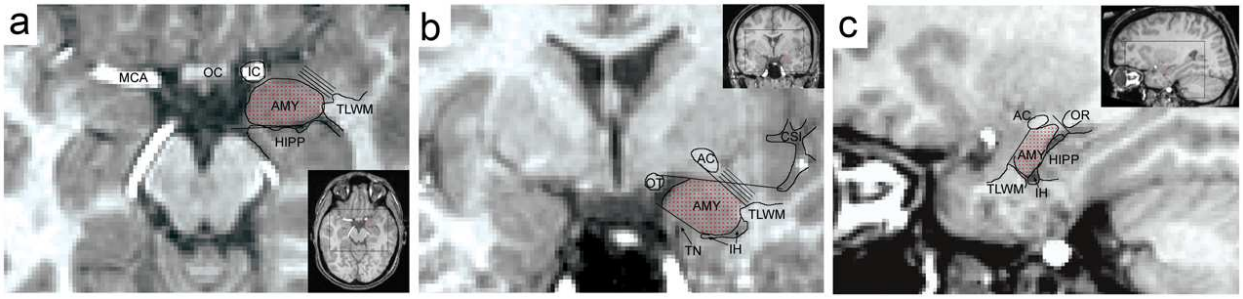

Figure 1. Amygdala manual segmentation at (a) axial (b) coronal and (c) midsagittal sections. The amygdala (AMY) was segmented using adjacent structures such as anterior commissure (AC), hippocampus (HIPP), inferior horn of lateral ventricle (IH), optic radiations (OR), optic tract (OT), temporal lobe white matter (TLWM) and tentorial notch (TN).

center. The radius of the sphere $\mathcal{M}_s$ is taken in such a way that the shortest distance between the sphere to the binary object $\mathcal{M}_a$ is 5mm. The final flattening map is definitely affected by the perturbation of the position of the sphere but since we are fixing it to be the mass center of surface for all amygdale, we do not need to worry about the perturbation effect.

The binary object $\mathcal{M}_a$ is assigned the value 1 while the enclosing sphere is assigned the value -1, i.e.

$$f(\mathcal{M}_a, \sigma) = 1 \text{ and } f(\mathcal{M}_s, \sigma) = -1 \tag{1}$$

for all $\sigma \in [0, \infty)$. The parameter σ is the diffusion time. $\mathcal{M}_a$ and $\mathcal{M}_s$ serve as a heat source and a heat sink respectively. Then we solve isotropic diffusion

$$\frac{\partial f}{\partial \sigma} = \Delta f \tag{2}$$

with the given boundary condition (1). Δ is the 3D Laplacian. When $\sigma \rightarrow$, the solution reaches the heat equilibrium state where the additional diffusion does not make any change in heat distribution. The heat equilibrium state is also obtained by letting $\frac{\partial f}{\partial \sigma} = 0$ and solving for the Laplace equation

$$\Delta f = 0 \tag{3}$$

with the same boundary condition. This will results in the equilibrium state denoted by $f(x, \sigma = \infty)$. Once we obtained the equilibrium state, we trace the path from the heat source to the heat sink for every mesh vertices on the isosurface of $\mathcal{M}_a$ using the gradient of the heat equilibrium $\nabla f(x, \infty)$. Similar formulation called the *Laplace equation method* has been used in estimating cortical thickness bounded by outer and inner cortical surfaces by establishing correspondence between two surfaces by tracing the gradient of the equilibrium state (Yezzi and Prince, 2001; Jones et al., 2006 ; Lerch and Evans, 2005).

The heat gradients form vector fields originating at the heat source and ending at the heat sink (Figure 2). The integral curve of the gradient field at a mesh vertex $p \in \partial\mathcal{M}_a$ establishes a smooth mapping from the mesh vertex to the sphere. The integral curve τ is obtained by solving a system of differential equations

$$\frac{d\tau}{dt}(t) = \nabla f(\tau(t), \infty)$$

with $\tau(t = 0) = p$. The integral curve approach is a widely used formulation in tracking white matter fibers using diffusion tensors (Basser et al., 2000; Lazar et al., 2003). These methods rely on discretizing the differential equations using the Runge-Kutta method; however, the such computation intensive approach is not needed here. Instead of directly computing the gradient field $\nabla f(x, \infty)$, we computed the level sets $f(x, \infty) = c$ of the equilibrium state corresponding to for varying c between -1 and 1. The integral curve is then obtained by finding the shortest path from one level set to the next level set and connecting them together in a piecewise fashion. This is done in an iterative fashion as shown in Figure 2, where five level sets corresponding to the values $c = 0.6, 0.2, -0.2, -0.6, -1.0$ are used to flatten the amygdala surface. Once we obtained the spherical mapping, we can then project the angles (θ, φ) onto $\partial\mathcal{M}_a$ and the two angles serve as the underlying parameterization for the weighted spherical harmonic representation.

For the proposed flattening method to work, the binary object has to be close to star-shape or convex. For shapes with a more complex structure, the gradient lines that correspond to neighboring nodes on the surface will fall within one voxel in the volume, creating singularities in mapping to the sphere. Other more complex mapping methods such as conformal mapping (Angenent et al., 1999; Gu et al., 2004; Hurdal and Stephenson, 2004) use the complexity to avoid this problem but more numerically demanding. On the other hands, our approach is simpler and more computationally efficient because it works for a limited class of shapes.

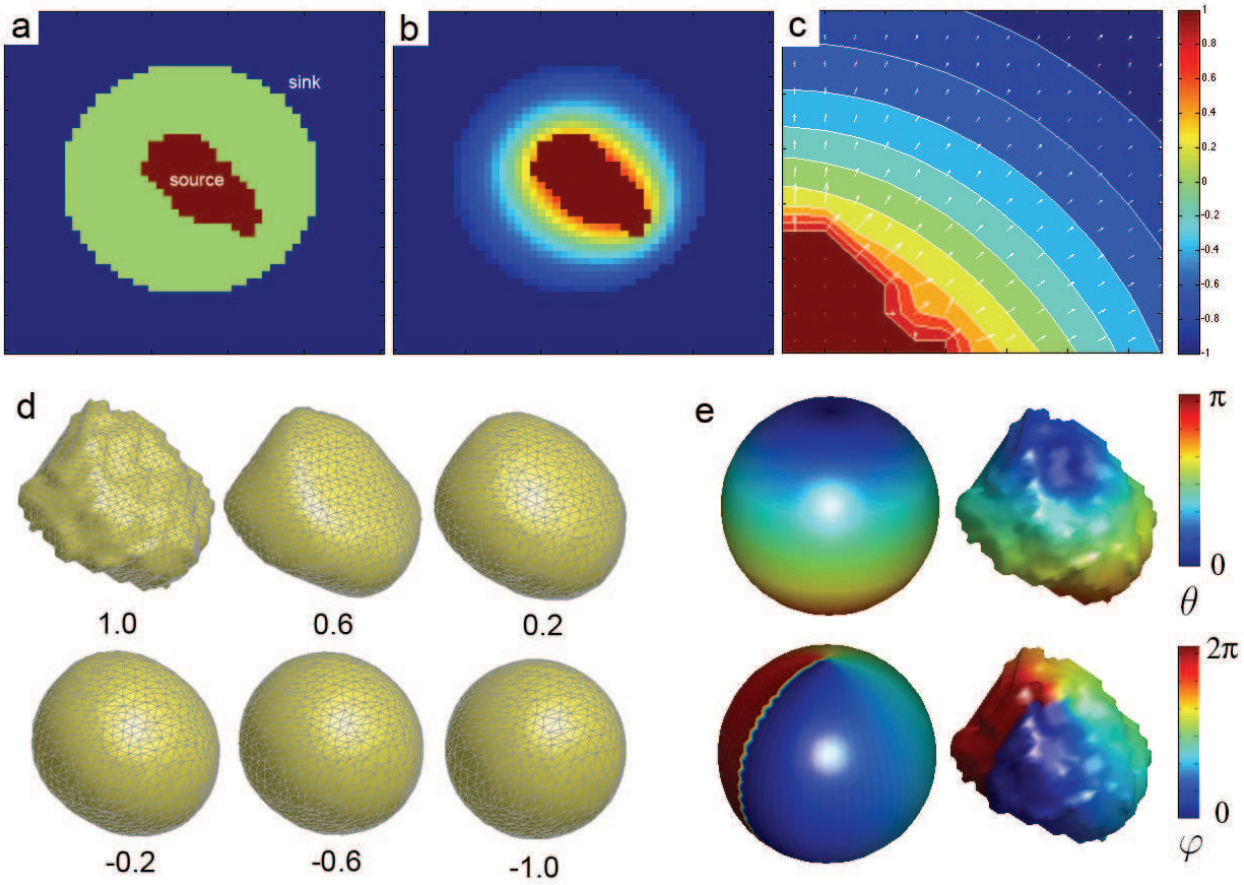

Figure 2. (a) The heat source (amygdala) is assigned value 1 while the heat sink is assigned the value -1. The diffusion equation is solved with these boundary condition. (b) After a sufficient number of iterations, the equilibrium state $f(x, \infty)$ is reached. (c) The gradient field $\nabla f(x, \infty)$ shows the direction of heat propagation from the source to the sink. The integral curve of the gradient field is computed by connecting one level set to the next level sets of $f(x, \infty)$. (d) Amygala surface flattening is done by tracing the integral curve at each mesh vertex. The numbers $c = 1.0, 0.6, \cdots, -1.0$ correspond to the level sets $f(x, \infty) = c$. (e) Amygdala surface parameterization using the angles (θ, φ). The point $\theta = 0$ corresponds to the north pole of a unit sphere.

2.2 *Weighted Spherical Harmonic Representation*

The parameterized amygdala surfaces, in terms of spherical angles θ, φ, are further expressed using the weighted spherical harmonic representation (Chung et al., 2007), which represent surface coordinate functions as a weighted linear combination of spherical harmonics. Chung et al. (2007) introduces the representation and the iterative parameter estimation technique called the *iterative residual fitting* (IRF) algorithm for representing extremely large meshes. The automatic degree selection procedure was also introduced but for the completeness of our paper, the method is given in section 2.3.

The mesh coordinates for the object surface $\partial\mathcal{M}_a$ are parameterized by the angles $\Omega = (\theta, \varphi) \in [0, \pi] \otimes [0, 2\pi)$ as

$$p(\theta, \varphi) = (p_1(\theta, \varphi), p_2(\theta, \varphi), p_2(\theta, \varphi)).$$

The weighted spherical harmonic representation is given by

$$p(\theta, \varphi) = \sum_{l=0}^{k} \sum_{m=-l}^{l} e^{-l(l+1)\sigma} f_{lm} Y_{lm}(\theta, \varphi),$$

where

$$f_{lm} = \int_{\theta=0}^{\pi} \int_{\varphi=0}^{2\pi} p(\theta, \varphi) Y_{lm}(\theta, \varphi) \ \sin\theta d\theta d\varphi$$

are the spherical harmonic coefficient vectors and Y_{lm} are spherical harmonics of degree l and order m defined as

$$Y_{lm} = \begin{cases} c_{lm} P_l^{|m|}(\cos\theta) \sin(|m|\varphi), & -l \leq m \leq -1, \\ \frac{c_{lm}}{\sqrt{2}} P_l^{|m|}(\cos\theta), & m = 0, \\ c_{lm} P_l^{|m|}(\cos\theta) \cos(|m|\varphi), & 1 \leq m \leq l, \end{cases}$$

where $c_{lm} = \sqrt{\frac{2l+1}{2\pi} \frac{(l-|m|)!}{(l+|m|)!}}$ and P_l^m is the *associated Legendre polynomial* of order m (Courant and Hilbert, 1953). The associated Legendre polynomial is given by

$$P_l^m(x) = \frac{(1-x^2)^{m/2}}{2^l l!} \frac{d^{l+m}}{dx^{l+m}} (x^2 - 1)^l, \ x \in [-1, 1].$$

The first few terms of the spherical harmonics are

$$Y_{00} = \frac{1}{\sqrt{4\pi}}, Y_{1,-1} = \sqrt{\frac{3}{4\pi}} \sin\theta \sin\varphi,$$
$$Y_{1,0} = \sqrt{\frac{3}{4\pi}} \cos\theta, Y_{1,1} = \sqrt{\frac{3}{4\pi}} \sin\theta \cos\varphi$$

and they are displayed in Figure 4.

Many previous imaging and shape modeling literature have used the complex-valued spherical harmonics (Bulow, 2004; Gerig et al., 2001; Gu et al., 2004; Shen et al., 2004), but we have only used real-valued spherical harmonics (Courant and Hilbert, 1953; Homeier and Steinborn, 1996) throughout the paper for the convenience in setting up a real-valued stochastic model. The relationship between the real- and complex-valued spherical harmonics is given in Blanco et al. (1997), and Homeier and Steinborn (1996). The complex-valued spherical harmonics can be transformed into real-valued spherical harmonics using an unitary transform. The coefficients f_{lm} are estimated by solving a system of linear equations. Given mesh coordinates $q(\Omega_j)$ at the angle Ω_j, we have

$$q(\Omega_j) = \sum_{l=0}^{k} \sum_{m=-l}^{l} e^{-l(l+1)\sigma} f_{lm} Y_{lm}(\Omega_j).$$

The linear equations are solved in the least squares fashion (Chung et al., 2007; Gerig et al., 2001; Shen et al., 2004).

One important property of the weighted spherical harmonic representation that is relevant to our study is that the representation is heat kernel smoothing (Chung et al., 2005). In the subsequent multivariate linear modeling, some sort of kernel smoothing is necessary before the random field theory based multiple comparison correction is performed. The connection toward heat kernel smoothing was first given in Chung et al. (2007) so here we briefly explain it.

On a unit sphere, the heat kernel is defined as

$$K_\sigma(\Omega, \Omega') = \sum_{l=0}^{\infty} \sum_{m=-l}^{l} e^{-l(l+1)\sigma} Y_{lm}(\Omega) Y_{lm}(\Omega'). \tag{4}$$

The heat kernel is symmetric and positive definite and the *bandwidth* σ controls the dispersion of the kernel. We define *heat kernel smoothing* of coordinates p as the convolution

$$K_\sigma * p(\Omega) = \int_{S^2} K_\sigma(\Omega, \Omega') p(\Omega') \, d\mu(\Omega'). \tag{5}$$

By substituting (4) into equation (5) and rearranging the integral with the summation, we can show that heat kernel smoothing is identical to the weighted spherical harmonic

representation:

$$K_\sigma * f(\Omega) = \sum_{l=0}^{\infty} \sum_{m=-l}^{l} e^{-l(l+1)\sigma} \langle f, Y_{lm} \rangle Y_{lm}(\Omega), \tag{6}$$

Hence, the weighted Fourier representation should inherit all the properties of kernel-based smoothing.

2.3 *Degree Selection*

Since it is impractical to sum the representation to infinity, we need a rule for truncating the series expansion. Given the bandwidth of heat kernel, we automatically determine if increasing degree k has any effect on the goodness of the fit of the representation. In all spherical harmolnic literature (Gerig et al., 2004; Gerig et al., 2001 ; Gu et al., 2004; Shen and Chung, 2006; Shen et al., 2004), the truncation degree is simply selected based on a pre-specified error bound. On the other hand, our proposed statistical framework does not depend on the pre-specified deterministic error bound but based statistical error, i.e. type-I error.

Although increasing the degree increases the goodness-of-fit of the representation, it also increases the number of coefficients to be estimated quadratically. It is necessary to find the optimal degree where the goodness-of-fit and the number of parameters balance out. Consider the following k-th degree reconstruction error model:

$$p(\Omega_i) = \sum_{l=0}^{k-1} \sum_{m=-l}^{l} e^{-l(l+1)\sigma} f_{lm} Y_{lm}(\Omega_i) + \sum_{m=-k}^{k} e^{-k(k+1)\sigma} f_{km} Y_{km}(\Omega_i) + \epsilon(\Omega_i) \tag{7}$$

at each mesh vertex Ω_i with a zero mean Gaussian noise. We test if adding the k-th degree terms to the $k-1$-th degree model is statistically significant by formally testing

$$H_0 : f_{k,-k} = \cdots = f_{k,k} = 0.$$

Let E_0 be the sum of squared residual corresponding to the reduced model while E be that of the full model. Under H_0, the test statistic is the F statistic

$$F = \frac{(E_0 - E)/(2k+1)}{E_0/(n-(k+1)^2)}$$

which is distributed as the F-distribution with $2k+1$ and $n-(k+1)^2$ degrees of freedom. At each degree, we compute the corresponding p-value and stop increasing the degree if it

is smaller than pre-specified significance $\alpha = 0.01$. For bandwidths $\sigma = 0.01, 0.001, 0.0001$, the approximate optimal degrees are 18, 42 and 78 respectively. In our study, we have used $k = 42$ degree representation corresponding to bandwidth $\sigma = 0.001$. The bandwidth 0.01 smoothes out too much local details while the bandwidth 0.0001 introduces too much voxel discretization error into the representation.

2.4 *Reduction of Gibbs Phenomenon*

The proposed *weighted spherical harmonic representation* fixes the Gibbs phenomenon (ringing effects) associated with the traditional Fourier descriptors and spherical harmonic representation (Brechbuhler et al., 1995; Gerig et al., 2001; Gu et al., 2004; Kelemen et al., 1999; Shen et al., 2004) by weighting the series expansion with exponential weights. The exponential weights make the representation converge faster and reduces the amount of ringing artifacts. The Gibbs phenomenon often arises in Fourier series expansion of discrete data.

The phenomenon was named after American physicist Josiah Willard Gibbs although it was was first observed by a mathematician Henry Willbraham in 1848 (Wilbraham, 1848). Josiah Willard Gibbs rediscovered the phenomenon as mathematical in 1899 (Gibbs, 1898). Later mathematician Maxime Bocher named it the Gibbs phenomenon and gave precise mathematical analysis in 1906. The Gibbs phenomenon associated with spherical harmonics were first observed by Herman Weyl in 1910 (Weyl, 1910). The history and the overview of Gibbs phenomenon can be found in several literature (Gelb, 1997; Gottlieb and Shu, 1997; Hewitt and Hewitt, 1979).

In representing a piecewise continuously differentiable data using the Fourier series, the overshoot of the series happens at a jump discontinuity. The overshoot does not decease as the number of terms increases in the series expansion, and it converges to a finite limit related to the Gibbs constant. To numerically quantify the amount of overshoot, we define the *overshoot* as the maximum of L_2 norm of coordinate difference between the original (p) and reconstructed (q) surfaces:

$$\sup_{(\theta,\varphi)\in S^2} \|q(\theta,\varphi) - p(\theta,\varphi)\|.$$

If surface coordinates are abruptly changing or their derivatives are discontinuous, the Gibbs

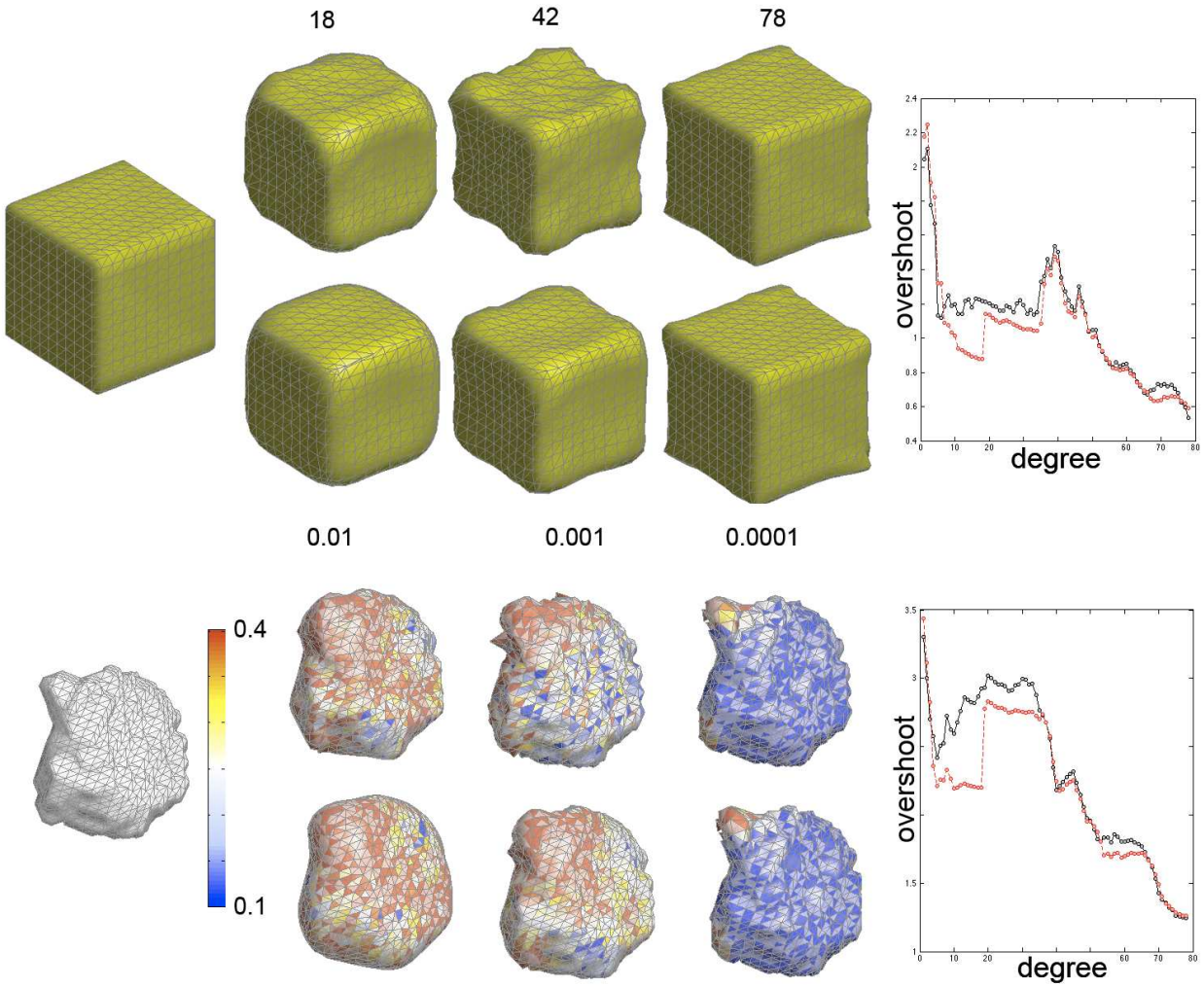

Figure 3. The first (third) row shows the significant Gibbs phenomenon in the spherical harmonic representation of a cube (left amygdala) for various degrees $k = 18, 42, 78$. The second (fourth) row is the weighted spherical harmonic representation at the same degree but with bandwidth $\sigma = 0.01, 0.001, 0.0001$ respectively. The color scale in the third and last rows are the absolute errors between the original and reconstructed amygdale. In almost all degrees, the traditional spherical harmonic representation shows more prominent Gibbs phenomenon compared to the weighted version. The plots display the amount of overshoot for the traditional representation (black) and the weighted version (red).

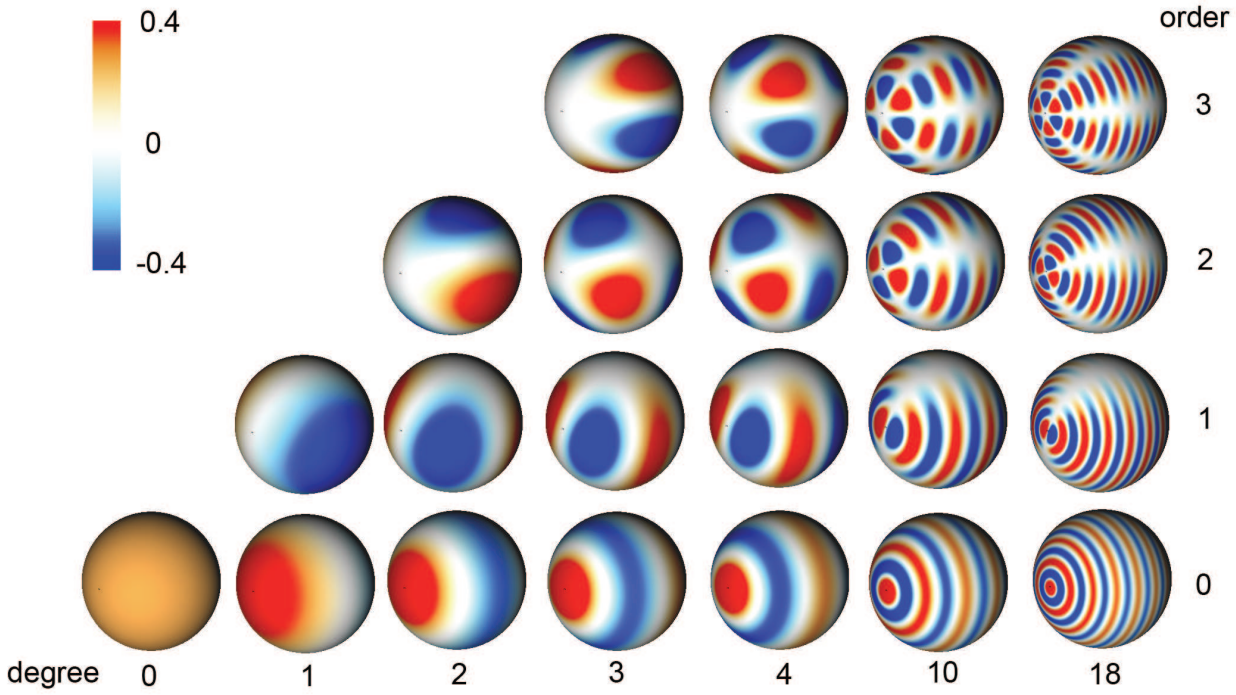

Figure 4. Spherical harmonic basis for various degree and order. Only nonnegative orders are shown. For the l-th degree, there are $2l + 1$ different orders. The spherical harmonic representation construct a function defined on a sphere as a linear combination of this basis.

phenomenon will severely distort the surface shape and the overshoot will never converge to zero.

We have reconstructed a cube and a left amygdala with various degree presentation and the bandwidth showing more ringing artifacts and overshoot in the traditional representation compared to the proposed weighted version. The color scale in the third and fourth rows are the absolute errors between the original and reconstructed amygdale. The exponentially decaying weights make the representation converge faster and reduce the Gibbs phenomenon significantly. Figure 3 shows the comparison of overshoots between the two representations. The plots display the amount of overshoot for the traditional representation (black) and the weighted version (red). The weighted spherical harmonic representation shows less amount of overshoot compared to the traditional technique. In particular, we observe a sharp peak sticking out, due to the overshoot, in the 42-degree traditional representation of the amygdala.

2.5 *Surface Normalization and Resampling*

Once object surfaces are represented with weighted spherical harmonics, we need to establish surface correspondence across different surfaces for the subsequent statistical analysis. However, it is computationally difficult to establish the correspondence across different meshes since any two triangle meshes will have different mesh topology, i.e. mesh connectivity. For instance, the first surface in Figure 5-(a) has 1270 vertices and 2536 faces while the second surface has 1302 vertices and 2600 faces. The proposed weighted spherical harmonic representation can establish correspondence between topologically different meshes. The correspondence is established by matching the coefficient of spherical harmonics at the same degree and order. This correspondence is proven to be optimal in the least squares sense (Chung et al., 2007).

Denote the surface coordinates corresponding to the i-th surface as p^i. Then we have the weighted spherical harmonic representation

$$p^i(\Omega) = \sum_{l=0}^{k} \sum_{m=-l}^{l} e^{-l(l+1)\sigma} f^i_{lm} Y_{lm}(\Omega), \tag{8}$$

where f^i_{lm} are the spherical harmonic coefficient vectors. There are total $(k+1)^2 \times 3$ coefficients to be estimated using the least squares method. Since the representation is continuously defined in any $\Omega \in [0, \pi] \otimes [0, 2\pi)$, it is possible to resample the meshes using a topologically different spherical mesh. We have uniformly sampled the unit sphere and constructed a spherical mesh with 2563 vertices and 5120 faces. This spherical mesh serves as a common mesh topology for all surfaces. After the resampling, all surfaces will have the identical mesh topology as the spherical mesh, and the identical vertex indices will correspond across different surfaces (Figure 5-(c)). The idea of uniform mesh topology has been previously used as the basis of all MNI based cortical thickness analysis in a different context (Chung et al., 2003; Chung et al., 2005; MacDonald et al., 2000; Lerch and Evans, 2005 ; Taylor and Worsley, 2008; Worsley et al., 2004).

The proposed idea of surface normalization and resampling is further used to construct the average surface. We assume there are total n surfaces. The average surface $\overline{p}$ is given as

$$\overline{p} = \frac{1}{n} \sum_{i=1}^{n} \sum_{l=0}^{k} \sum_{m=-l}^{l} e^{-l(l+1)\sigma} f^i_{lm} Y_{lm}. \tag{9}$$

In our study, the average left and right amygdala templates are constructed by averaging the spherical harmonic coefficients of all 24 control subjects. The template surfaces serve as the reference coordinates for projecting the subsequent statistical parametric maps (Figure 8 and 9).

2.6 *Multivariate Linear Models*

Multivariate linear models (Anderson, 1984; Taylor and Worsley, 2008; Worsley et al., 2004) generalize widely used univariate general linear models (Worsley et al., 1996) by incorporating vector valued response and explanatory variables. The weighted spherical harmonic representation of surface coordinates will be taken as the response variable P. Consider the following multivariate linear model at each fixed (θ, φ)

$$P_{n\times 3} = X_{n\times p}B_{p\times 3} + Z_{n\times r}G_{r\times 3} + U_{n\times 3}\Sigma_{3\times 3}, \tag{10}$$

where $P = (p^{1\prime}, p^{2\prime}, \cdots, p^{n\prime})'$ is the matrix of weighted spherical harmonic representation, X is the matrix of contrasted explanatory variables, and B is the matrix of unknown coefficients. Nuisance covariates are in the matrix Z and the corresponding coefficients are in the matrix G. The subscripts denote the dimension of matrices. The components of Gaussian random matrix U are zero mean and unit variance. Σ accounts for the covariance structure of coordinates. Then we are interested in testing the null hypothesis

$$H_0 : B = 0.$$

For the reduced model corresponding to $B = 0$, the least squares estimator of G is given by

$$\widehat{G}_0 = (Z'Z)^{-1}Z'P.$$

The residual sum of squares of the reduced model is

$$E_0 = (P - Z\widehat{G}_0)'(P - Z\widehat{G}_0)$$

while that of the full model is

$$E = (P - X\widehat{B} - Z\widehat{G})'(P - X\widehat{B} - Z\widehat{G}).$$

Note that $\widehat{G}$ is different from $\widehat{G}_0$ and estimated directly from the full model. By comparing how large the residual E is against the residual E_0, we can determine the significance of

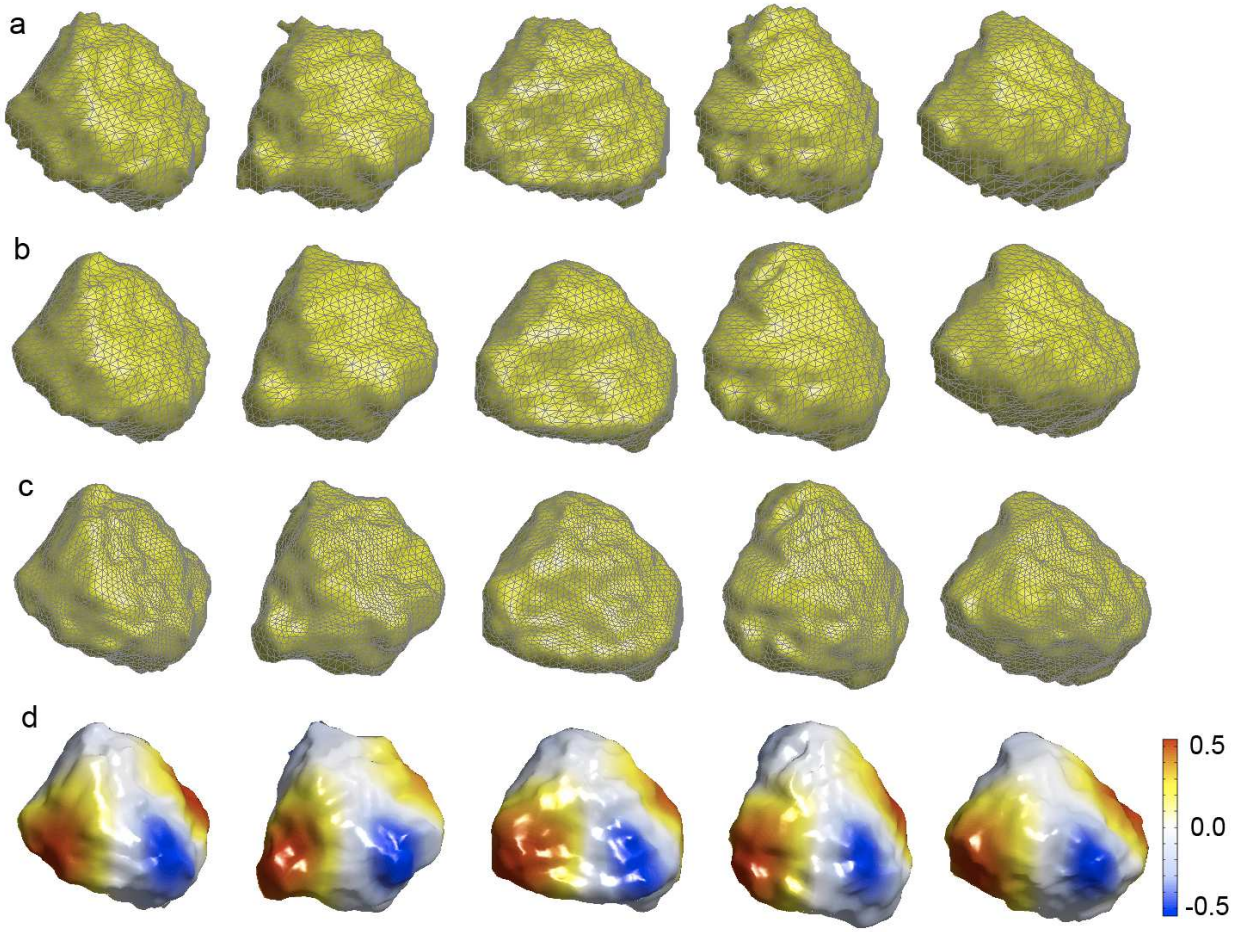

Figure 5. (a) Five representative left amygdala surfaces. (b) 42 degree weighted spherical harmonic representation. Surfaces have different mesh topology. (c) However, meshes can be resampled in such a way that all meshes have identical topology with exactly 2562 vertices and 5120 faces. Identically indexed mesh vertices correspond across different surfaces in the least squares fashion. (d) Spherical harmonic basis Y_{22} is projected on each amygdala to show surface correspondence. Note that the red colored left most corners more or less align properly.

coefficients B. However, since E and E_0 are matrices, we take a function of eigenvalues of EE_0^{-1} as a statistic. For instance, *Lawley-Hotelling trace* is given by the sum of eigenvalues while *Roy's maximum root* R is the largest eigenvalue. In the case there is only one eigenvalue, all these multivariate test statistics simplify to *Hotelling's T-sqaure* statistic. The Hotelling's T-square statistic has been widely used in modeling 3D coordinates and deformations in brain imaging (Cao and Worsley, 1999; Chung et al., 2001; Gaser et al., 1999; Joshi, 1998; Thompson et al., 1997). The random field theory for Hotelling's T-square statistic has been available for a while (Cao and Worsley, 1999). However, the random field theory for the Roy's maximum root has not been developed until recently (Taylor and Worsley, 2008; Worsley et al., 2004).

The inference for Roy's maximum root is based on the Roy's union-intersection principle (Roy, 1953), which simplifies the multivariate problem to a univariate linear model. Let us multiply an arbitrary constant vector $\nu_{3\times 1}$ on both sides of (10):

$$P\nu = XB\nu + ZG\nu + U\Sigma\nu. \tag{11}$$

Obviously (11) is a usual univariate linear model with a Gaussian noise. For the univariate testing on $B\nu = 0$, the inference is based on the F statistic with p and $n - p - r$ degrees of freedom, denoted as F_ν. Then Roy's maximum root statistic can be defined as $R = \max_\nu F_\nu$. Now it is obvious that the usual random field theory can be applied in correcting for multiple comparisons. The only trick is to increase the search space, in which we take the supreme of the F random field, from the template surface to much higher dimension to account for maximizing over ν as well.

2.7 *SurfStat*

SurfStat package was developed by K.J. Worsley utilizing a model formula and avoids the explicit use of design matrices and contrasts, which tend to be a hinderance to most end users not familiar with such concepts. SurtStat can import MNI (MacDonald et al., 2000), FreeSurfer (`surfer.nmr.mgh.harvard.edu`) based cortical mesh formats as well as other volumetric image data. The model formula approach is implemented in many statistics packages such as Splus (`www.insightful.com`) R (`www.r-project.org`) and SAS (`www.sas.com`). These statistics packages accept a linear model like

$$\texttt{P} = \texttt{Group} + \texttt{Age} + \texttt{Brain}$$

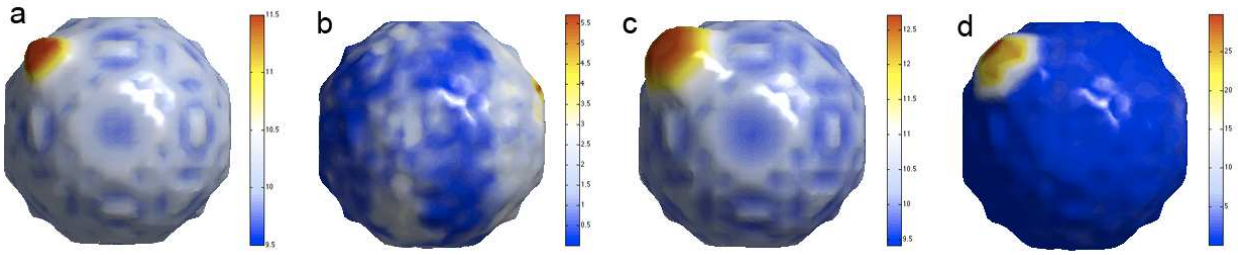

Figure 6. Simulation results. (a) small bump of height 1.5mm was added to a sphere of radius 10 mm. (b) T-statistic of comparing randomly simulated 20 spheres and 20 bumped spheres showing no group difference ($p < 0.35$). (c) small bump of height 3mm was added to a sphere of radius 10mm. (d) T-statistic of comparing randomly simulated 20 spheres and 20 bumped spheres showing significant group difference ($p < 0.0003$).

as the direct input for linear modeling avoiding the need to explicitly state the design matrix. `P` is a $n \times 3$ matrix of coordinates of weighted spherical harmonic representation, `Age` is the age of subjects, `Brain` is the total brain volume of subject and `Group` is the categorical group variable (0=control, 1 = autism). This type of model formula has yet to be implemented in widely used SPM or AFNI packages.

2.8 *Simulation Study*

We have performed two simulation studies to determine if the proposed pipeline can detect a small artificial bump. A similar bump test was done in Yu et al. (2007) for testing the effectiveness of a spherical wavelet representation. In the first simulation, we have generated the binary mask of a sphere with radius 10mm. Then we obtained the weighted spherical harmonic representation (6) of the sphere with $\sigma = 0.001$ and degree $k = 42$. Taking the estimated coefficients f_{lm} as the ground truth, we simulated 20 spheres (group A) by putting randomness in the spherical harmonic coefficients as $N(f_{lm}, (f_{lm}/20)^2)$. The standard deviation is taken as the 20th of the mean signal. We have also given a bump of height 1.5mm to the sphere and simulated 20 bumped sphere (Figure 6 -(a)). Two groups of surfaces are fed into the multivariate linear model testing for the group effect. The resulting T-statistic map is projected on the average of 40 simulated surfaces (Figure 6-(b)). Since the bump is so small with respect to the noise level, we did not detect any the bump ($p < 0.35$).

In the second simulation, we increased the height of the bump to 3mm (Figure 6-(c)) and repeated the first simulation. The resulting T-statistic map is projected on the average of 40 simulated surfaces (Figure 6-(d)). Unlike the first simulation study, we have detected the bump in yellow and red regions ($p < 0.0003$). These experiments demonstrate that the proposed framework works for detecting sufficiently large shape difference, and further indicates that what we detected in the real amygdala application is of sufficiently large shape difference.

3. Application: Amygdala Shape Modeling in Autism

3.1 *Image and Data Acquisition*

High resolution T1-weighted magnetic resonance images (MRI) were acquired with a GE SIGNA 3-Tesla scanner with a quadrature head coil with 240 × 240 mm field of view and 124 axial sections. Details on image acquisition parameters are given in Dalton et al. (2005) and Nacewicz et al. (2006). T2-weighted images were used to smooth out inhomogeneities in the inversion recovery-prepared images using FSL (`www.fmrib.ox.ac.uk/fsl`). Total 22 autistic and 24 normal control MRI were acquired. Subjects were all males aged between 8 and 25 years. The Autism Diagnostic Interview-Revised (Lord et al., 1994) was used for diagnoses by trained researchers K.M. Dalton and B.M. Nacewicz (Dalton et al., 2005).

MRIs were first reoriented to the pathological plane for optimal comparison with anatomical atlases (Convit et al., 1999). Image contrast was matched by alignment of white and gray matter peaks on intensity histograms. Manual segmentation was done by a trained expert B.M. Nacewicz who has been blind to the diagnoses (Nacewicz et al., 2006). The manual segmentation also involves refinement through plane-by-palne comparison with ex vivo atlas sections (Mai et al., 1997). The reliability of the manual segmentation protocol was validated by two raters on 10 amygdale resulting in interclass correlation of 0.95 and the spatial reliability (intersection over union) average of 0.84. The total brain volume was also computed using an automated threshold-based connected voxel search method, and manually edited afterwards to ensure proper removal of skull, eye regions, brainstem and cerebellum. Figure 1 shows the manual segmentation of an amygdala in three different cross sections. The amygdala (AMY) was traced in detail using various adjacent structures such as anterior commissure (AC), hippocampus (HIPP), inferior horn of lateral ventricle (IH),

optic radiations (OR), optic tract (OT), temporal lobe white matter (TLWM) and tentorial notch (TN).

A subset of subjects (10 controls and 12 autistic) went through a face emotion recognition task consisting of showing 40 standardized pictures of posed facial expressions (8 each of happy, angry and sad, and 16 neutral) (Dalton et al., 2005). Subjects were required to press a button distinguishing neutral from emotional faces. The faces were black and white pictures taken from the Karolinska Directed Emotional Faces set (Lundqvist et al., 1998). The faces were presented using E-Prime software (`www.pstnet.com`) allowing for the measurement of response time for each trial. iView system with a remote eye-tracking device (SensoMotoric Instruments, `www.smivision.com`) was used at the same time to measure gaze fixation duration on eyes and faces during the task. The system records eye movements as the gaze position of the pupil over a certain length of time along with the amount of time spent on any given fixation point. It has been hypothesized that subjects with autism should exhibit diminished eye fixation duration relative to face fixation duration. If there is no confusion, we will simply refer *gaze fixation* as the ratio of durations fixed on eyes over faces. Note that this is a unitless measure. Our study enables us to show that abnormal gaze fixation duration is correlated with amygdala shape in spatially localized regions.

3.2 *Amygdala Volumetry*

We have counted the number of voxels in amygdala segmentation and computed the volume of both left and right amygdale. The volumes for control subjects ($n = 22$) are left $1892 \pm 173\text{mm}^3$, right $1883 \pm 171\text{mm}^3$. The volumes for autistic subjects ($n = 24$) are left $1858 \pm 182\text{mm}^3$, right $1862 \pm 181\text{mm}^3$. The volume difference between the groups is not statistically significant based on the two sample t-test ($p = 0.52$ for left and 0.69 for right). Previous amygdala volumetry studies in autism have been inconsistent (Aylward et al., 1999; Haznedar et al., 2000; Nacewicz et al., 2006; Pierce et al., 2001; Schumann et al., 2004; Sparks et al., 2002). Aylward et al. (1999) and Pierce et al. (2001) reported that significantly smaller amygdala volume in the autistic subjects while Howard et al. (2000) and Sparks et al. (2002) reported larger volume. Haznedar et al. (2000) and Nacewicz et al. (2006) found no volume difference. These inconsistency might be due to the lack of control for brain size and age in statistical analysis (Schumann et al., 2004). The effect of age and the total brain volume on amygdala volume can be seen in Figure 7. Therefore, it is necessary to test group difference

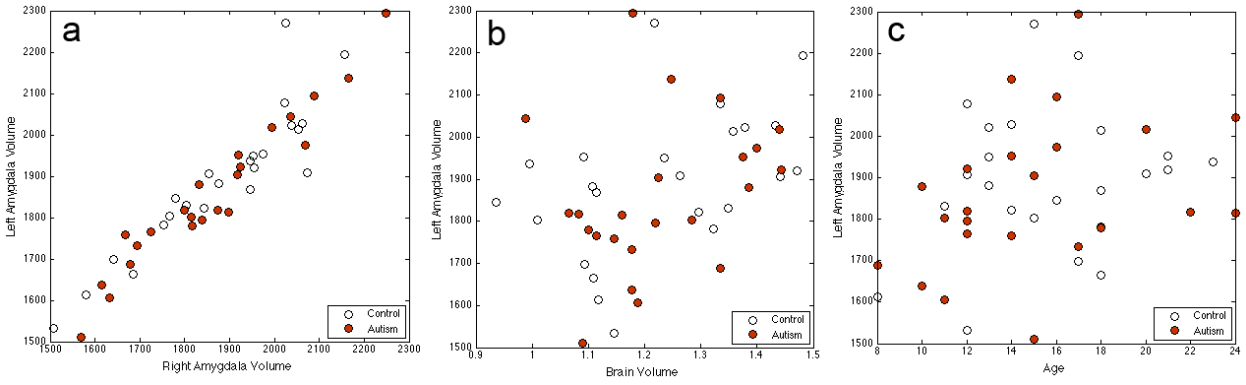

Figure 7. Scatter plots of left amygdala volume (vertical axis) vs. (a) right amygdala volume (b) total brain volume and (c) age showing significant confounding effect of total brain volume and age on amygdala volume. Any statistical analysis on amygdala volume and shape needs to account for brain volume and age.

while accounting for the total brain volume and age. We did not detect any group difference in amygdala volume for both left ($p = 0.66$) and right ($p = 0.53$) amygdale. The testing was done using SurfStat.

3.3 *Local Shape Difference*

From the amygdala volumetry result, it is still not clear if shape difference might be still present within amygdala. It is possible to have no volume difference while having significant shape difference. So we have performed multivariate linear modeling on the weighted spherical harmonic representation. We have tested the effect of group variable by comparing the sum of squared residuals of the full (`P=1+Group`) and the reduced (`P=1`) models, which resulted in the threshold of 26.99, which is far larger than the maximum F statistic value of 13.55 in Figure 8 (a). So we could not detect any shape difference in the left amygdala. For the right amygdala, the $\alpha = 0.1$ level thresholding is 26.64 which is far larger than the maximum F statistic value of 12.11. So again there is no statistically significant shape difference in the right amygdala.

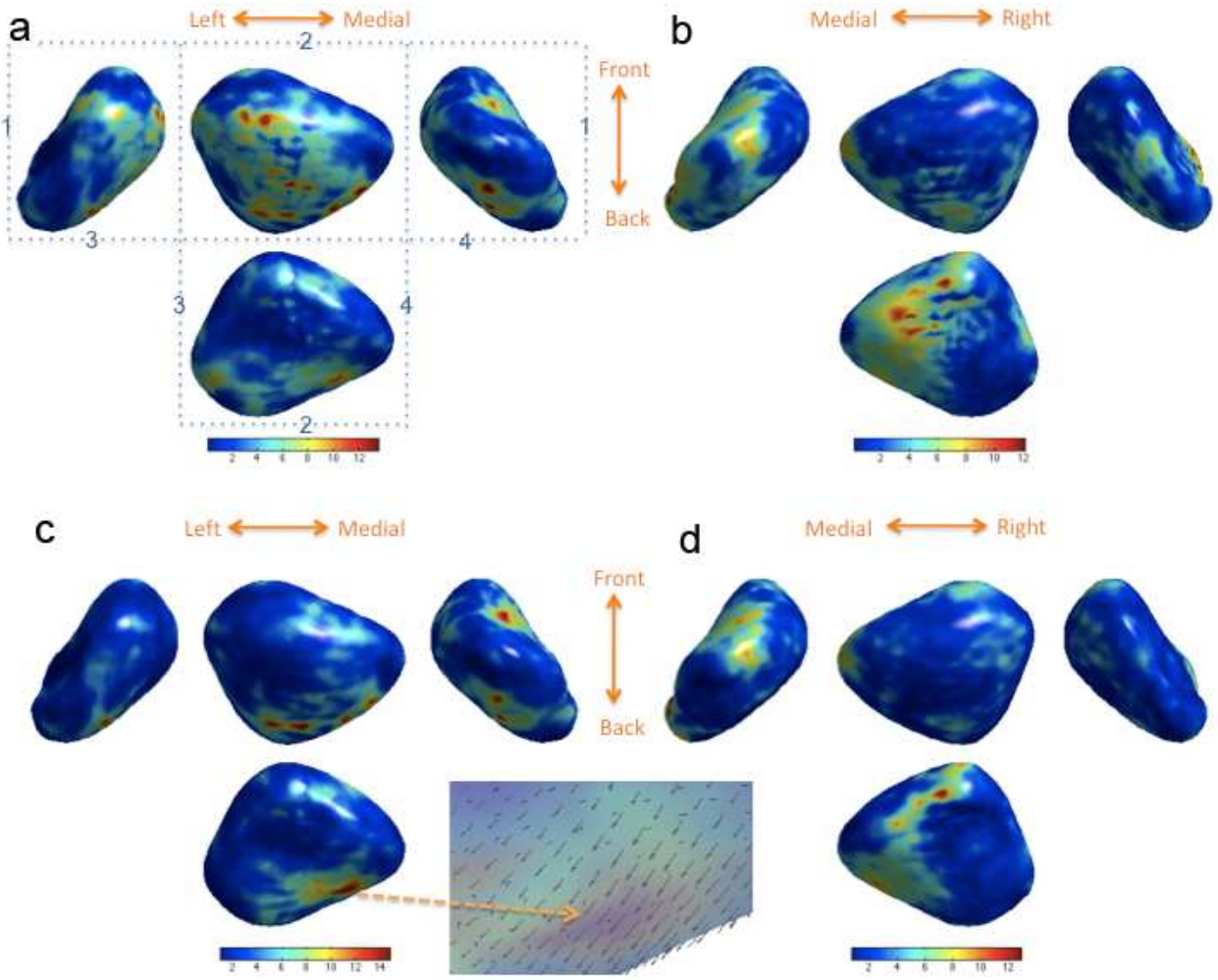

Figure 8. F statistic map of shape difference displayed on the average left amygdala (a) and right amygdala (b). We did not detect any significant difference at $\alpha = 0.1$. The left amygdala (a) is displayed in such a way that, if we fold along the dotted lines and connect the identically numbered lines, we obtain the 3D view of the amygdala. The top middle rectangle corresponds to the axial view obtained by observing the amygdala from the top of the brain. (c) and (d) show the F statistic map of shape difference accounting for age and the total brain volume. We have detected regions of shape difference in the left amygdala (red regions) ($p < 0.1$). The arrows in the enlarged area show the direction of shape difference (autism - control) indicating autistic subjects has larger amygdala in that area.

3.4 *Local Shape Difference Accounting for Age and Brain Size*

We have tested the effect of `Group` variable while accounting for age and the total brain volume by comparing the sum of squared residuals of the full (`P=Age+Brain+Group`) and the reduced (`P=Age+Brain`) models. The maximum F statistics are 14.77 (left) and 12.91 (right) while the threshold corresponding to the $\alpha = 0.1$ is 14.58 (left) and 14.61 (right). Hence, we still did not detect group difference in the right amygdala (Figure 8-c) while there is a localized region of group difference in the left amygdala (Figure 8-d). By computing the average surface coordinate difference (autism - control), we have determined the direction of shape difference. See the vector fields of the enlarged area in Figure . The outward direction implies that the autistic subjects has larger amygdale in the region.

3.5 *Brain and Behavior Association*

Among total 46 subjects, 10 control and 12 autistic subjects went through face emotion recognition task and gaze fixation `Fixation` was observed. The gaze fixation are 0.30 ± 0.17 (control) and 0.18 ± 0.16 (autism). Nacewicz et al. (2006) showed the gaze fixation duration correlate differently with amygdala volume between the two groups; however, it was not clear if the association difference is local or diffuse over all amygdala. So we have tested the significance of the interaction between `Group` and `Fixation` using multivariate linear models. The reduced model is

$$\texttt{P} = \texttt{Age} + \texttt{Brai} + \texttt{Group} + \texttt{Fixation}$$

while the full model is

$$\texttt{P} = \texttt{Age} + \texttt{Brain} + \texttt{Group} + \texttt{Fixation} + \texttt{Group} * \texttt{Fixation}$$

and we tested for the significance of the interaction `Group*Fixation`.

We have obtained regions of significant interaction in the both left ($p < 0.05$) and right ($p < 0.02$) amygdale (Figure 9). The largest cluster in the right amygdala shows highly significant interaction ($\max F = 65.68$, $p = 0.003$). The color bar in Figure 9-(b) has been thresholded at 40 for better visualization. The scatter plots of the z-coordinate of the displacement vector field vs. `Fixation` are shown at the two most significant clusters in each amygdala. The red lines are linear regression lines. The significance of interaction implies difference in regression slopes between groups in a multivariate fashion.

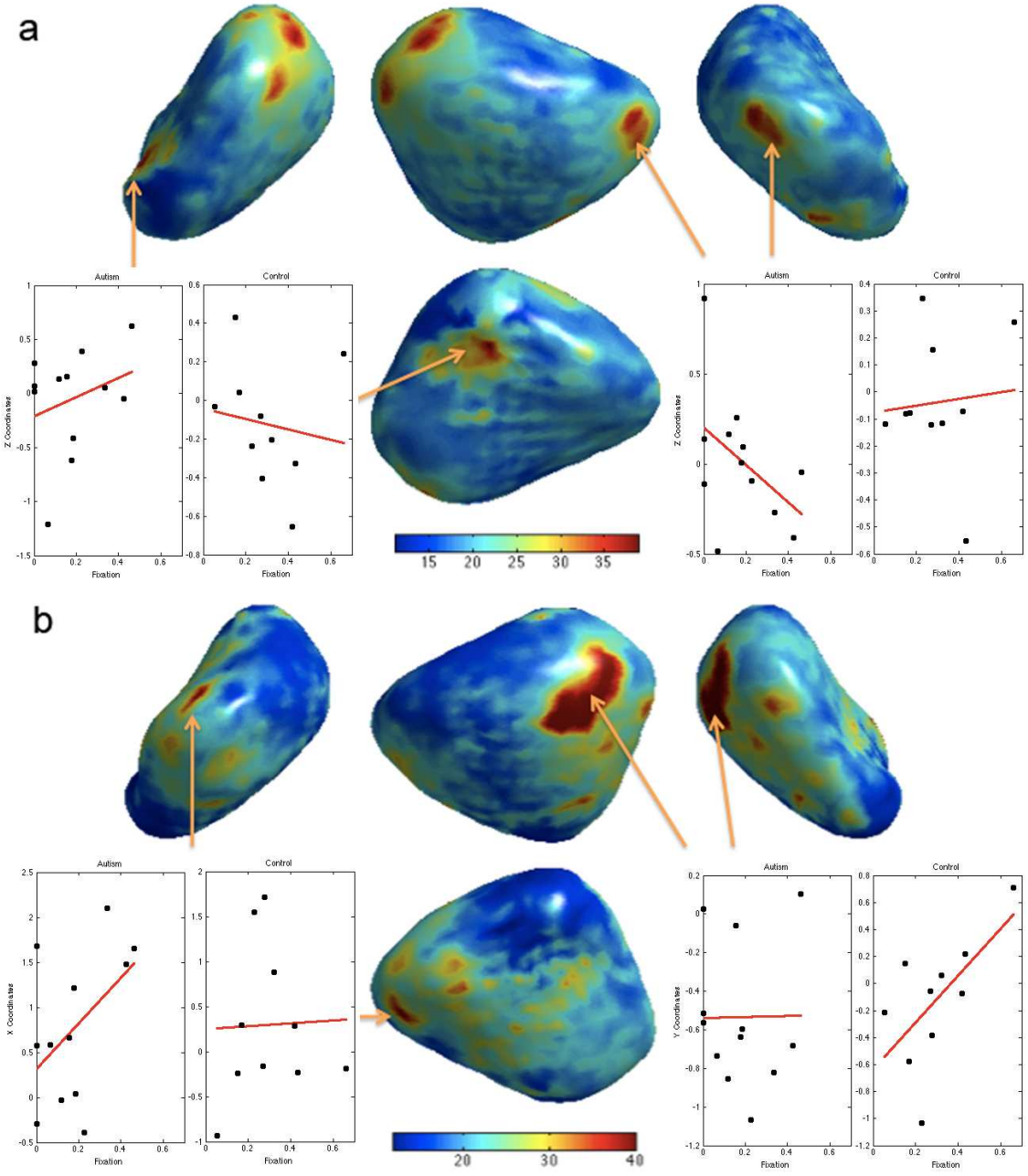

Figure 9. F statistic map of interaction between group and gaze fixation. Red regions show significant interaction for (a) left and (b) right amygdale. For better visualization, the color bar for the right amygdala (b) has been thresholded at 40 since the maximum F statistics at the largest cluster is 65.68 ($p = 0.003$). The scatter plots show the particular coordinate of the displacement vector from the average surface vs. gaze fixation. The red lines are regression lines.

4. Discussion

Summary. The paper proposed a unified multivariate linear modeling approach for a collection of binary objects and applied the method to amygdala shape analysis in autism. The coordinates of amygdala surfaces are smoothed and normalized using the novel weighted spherical harmonic representation. The main methodological contributions are the development of a new amygdala surface flattening technique, the weighted spherical harmonic representation, and the SurfStat package and accompanying publicly available codes that enables the first multivariate linear modeling on anatomical shapes.

Since surface data is inherently multivariate data, traditionally Hotelling's T-square approach has been used on surface coordinates in a group comparison. The proposed multivariate linear model generalizes the Hotelling's T-square approach so that we can construct more complicated statistical models. The model formula based multivariate linear modeling tool SurfStat is also available through a website. We have applied the proposed methods to 22 autistic subjects to test if there is localized shape difference within an amygdala. We were able to localize regions, mainly in the right amygdala, that shows differential association of gaze fixation with anatomy between the groups.

Anatomical Findings. Many MRI-based volumetric studies have shown inconsistent results in determining if there are any abnormal amygdala volume difference (Aylward et al., 1999; Howard et al., 2000; Haznedar et al., 2000; Pierce et al., 2001; Schumann et al., 2004; Sparks et al., 2002; Nacewicz et al., 2006). These studies focus on the total volume difference of amygdala obtained from MRI and was unable to determine if the volume difference is locally focused within the subregions of amygdala or diffuse over all regions.

Although we did not detect statistically significant shape difference within amygdala at level 0.05, we detected significant group difference of shape in relation to the gaze fixation duration mostly in the both lateral nuclei (largest clusters in Figure 9). The lateral nucleus receives information from the thalamus and cortex, and relay it to other subregions within the amygdala. Our finding is consistent with literature that reports that autistic subjects fail to activate the amygdala normally when processing emotional facial and eye expressions (Baron-Cohen et al., 1999; Critchley et al., 2000; Barnea-Goraly et al., 2004). A post-mortem study shows there are increased neuron-packing density of the medial, cortical and central nuclei, and medial and basal lateral nuclei of the amygdala in five autopsy cases (Courchesne, 1997).

Reduced fractional anisotropy is found in the temporal lobes approaching the amygdala bilaterally in a diffusion tensor imaging study (Barnea-Goraly et al., 2004).

The inconsistent amygdala volumetry results seem to be caused by the local volume and shape difference of the lateral nuclei that may or may not contribute to the total volume of amygdala. Further shape analysis on the white matter fiber tracts connecting the lateral nuclei would confirm the abnormal nature of lateral nucleus of the amygdala and its structural connection to other parts of the brain.

Methodological Limitations. There are few methodological limitations in our proposed study.

Surface flattening is based on tracing the streamline of the gradient of heat equilibrium. The proposed flattening technique is simple enough to be applied to various binary objects. However, for the proposed flattening method to work, the binary object has to be close to star-shape or convex. Theoretically, the solution to the Laplacian equation (3) is uniquely given and the heat gradient will never cross within the space between the inner and outer boundaries. However, for more complex structures like cortical surfaces, the gradient lines that correspond to neighboring nodes on the surface may fall within one voxel in the volume, creating overlapping nonsmooth mapping to the sphere. The overlapping problem can be avoided by subsampling the voxel grid in a much finer resolution but further methodological refinement is needed.

Although the proposed weighted spherical harmonic approach streamlines various image processing tasks such as smoothing, representation and registration within a unified mathematical representation, we did not compare the performance with other available shape representation techniques such as the medial representation (Pizer et al., 1999) and wavelets (Yu et al., 2007). This is the beyond the scope of the current paper and requires an additional comparative study.

Acknowledgment

The authors with to thank three anonymous reviewers for constructive comments. Also wish to thank Martin A. Styner of the department of Psychiatry and Computer Science of the University of North Carolina at Chapel Hill and Shubing Wang of Merck for various

discussions on spherical harmonic modeling and his ITK toolbox.

References

Anderson, T. (1984). *An Introduction to Multivariate Statistical Analysis*. Wiley., 2nd. edition.

Angenent, S., Hacker, S., Tannenbaum, A. and Kikinis, R. (1999). On the laplace-beltrami operator and brain surface flattening. *IEEE Transactions on Medical Imaging* **18**, 700–711.

Ashburner, J., Hutton, C., Frackowiak, R. S. J., Johnsrude, I., Price, C. and Friston, K. J. (1998). Identifying global anatomical differences: Deformation-based morphometry. *Human Brain Mapping* **6**, 348–357.

Aylward, E., Minshew, N., Goldstein, G., Honeycutt, N., Augustine, A., Yates, K., Bartra, P. and Pearlson, G. (1999). Mri volumes of amygdala and hippocampus in nonmentally retarded autistic adolescents and adults. *Neurology* **53**, 2145–2150.

Barnea-Goraly, N., Kwon, H., Menon, V., Eliez, S., Lotspeich, L. and Reiss, A. (2004). White matter structure in autism: preliminary evidence from diffusion tensor imaging. *Biological Psychiatry* **55**, 323–326.

Baron-Cohen, S., Ring, H., Wheelwright, S., Bullmore, E., Brammer, M., Sim-mons, A. and Williams, S. (1999). Social intelligence in the normal and autistic brain: An fMRI study. *Eur J Neurosci* **11**, 1891–1898.

Basser, P., Pajevic, S., Pierpaoli, C., Duda, J. and Aldroubi, A. (2000). In vivo tractography using dt-mri data. *Magnetic Resonance in Medicine* **44**, 625–632.

Blanco, M., Florez, M. and Bermejo, M. (1997). Evaluation of the rotation matrices in the basis of real spherical harmonics. *Journal of Molecular Structure: THEOCHEM* **419**, 19–27.

Brechbuhler, C., Gerig, G. and Kubler, O. (1995). Parametrization of closed surfaces for 3d shape description. *Computer Vision and Image Understanding* **61**, 154–170.

Bulow, T. (2004). Spherical diffusion for 3D surface smoothing. *IEEE Transactions on Pattern Analysis and Machine Intelligence* **26**, 1650–1654.

Cao, J. and Worsley, K. J. (1999). The detection of local shape changes via the geometry of

hotellings t2 fields. *Annals of Statistics* **27**, 925–942.

Chung, M., Dalton, K.M., L. S., Evans, A. and Davidson, R. (2007). Weighted Fourier representation and its application to quantifying the amount of gray matter. *IEEE Transactions on Medical Imaging* **26**, 566–581.

Chung, M., Robbins, S., Dalton, K.M., D. R. A. A. and Evans, A. (2005). Cortical thickness analysis in autism with heat kernel smoothing. *NeuroImage* **25**, 1256–1265.

Chung, M., Worsley, K., Paus, T., Cherif, D., Collins, C., Giedd, J., Rapoport, J., and Evans, A. (2001). A unified statistical approach to deformation-based morphometry. *NeuroImage* **14**, 595–606.

Chung, M., Worsley, K., Robbins, S., Paus, T., Taylor, J., Giedd, J., Rapoport, J. and Evans, A. (2003). Deformation-based surface morphometry applied to gray matter deformation. *NeuroImage* **18**, 198–213.

Collins, D. L., Paus, T., Zijdenbos, A., Worsley, K. J., Blumenthal, J., Giedd, J. N., Rapoport, J. L. and Evans, A. C. (1998). Age related changes in the shape of temporal and frontal lobes: An mri study of children and adolescents. *Soc. Neurosci. Abstr.* **24**, 304.

Convit, A., McHugh, P., Wolf, O., de Leon, M., Bobinkski, M., De Santi, S., Roche, A. and Tsui, W. (1999). Mri volume of the amygdala: a reliable method allowing separation from the hippocampal formation. *Psychiatry Res.* **90**, 113–123.

Courant, R. and Hilbert, D. (1953). *Methods of Mathematical Physics: Volume II.* Interscience, New York, english edition.

Courchesne, E. (1997). Brainstem, cerebellar and limbic neuroanatomical abnormalities in autism. *Current Opinion in Neurobiology* **7**, 269–278.

Critchley, H., Daly, E., Bullmore, E., Williams, S., T, V. A. and Robert-son, D. e. a. (2000). The functional neuroanatomy of social behaviour: Changes in cerebral blood ow when people with autistic disorder pro- cess facial expressions. *Brain* **123**, 2203–2212.

Csernansky, J., Wang, L., Joshi, S., Tilak Ratnanather, J. and Miller, M. (2004). Computational anatomy and neuropsychiatric disease: probabilistic assessment of variation and statistical inference of group difference, hemispheric asymmetry, and time-dependent change. *NeuroImage* **23**, 56–68.

Dalton, K., Nacewicz, B., Johnstone, T., Schaefer, H., Gernsbacher, M., Goldsmith, H., Alexander, A. and Davidson, R. (2005). Gaze fixation and the neural circuitry of face

processing in autism. *Nature Neuroscience* **8**, 519–526.

Fischl, B. and Dale, A. (2000). Measuring the thickness of the human cerebral cortex from magnetic resonance images. *PNAS* **97**, 11050–11055.

Gaser, C., Volz, H.-P., Kiebel, S., Riehemann, S. and Sauer, H. (1999). Detecting structural changes in whole brain based on nonlinear deformationsapplication to schizophrenia research. *NeuroImage* **10**, 107–113.

Gelb, A. (1997). The resolution of the gibbs phenomenon for spherical harmonics. *Mathematics of Computation* **66**, 699–717.

Gerig, G., Styner, M., Jones, D., Weinberger, D. and Lieberman, J. (2001). Shape analysis of brain ventricles using spharm. In *MMBIA*, pages 171–178.

Gerig, G., Styner, M. and Szekely, G. (2004). Statistical shape models for segmentation and structural analysis. In *Proceedings of IEEE International Symposium on Biomedical Imaging (ISBI)*, volume I, pages 467–473.

Gibbs, J. (1898). Fouriers series. *Nature* **59**, 200.

Golland, P., Grimson, W., Shenton, M. and Kikinis, R. (2001). Deformation analysis for shape based classification. *Lecture Notes in Computer Science* pages 517–530.

Gottlieb, D. and Shu, C. (1997). On the Gibbs phenomenon and its resolution. *SIAM Review* pages 644–668.

Gu, X., Wang, Y., Chan, T., Thompson, T. and Yau, S. (2004). Genus zero surface conformal mapping and its application to brain surface mapping. *IEEE Transactions on Medical Imaging* **23**, 1–10.

Haznedar, M., Buchsbaum, M., Wei, T., Hof, P., Cartwright, C. and Bienstock, C.A. Hollander, E. (2000). Limbic circuitry in patients with autism spectrum disorders studied with positron emission tomography and magnetic resonance imaging. *American Journal of Psychiatry* **157**, 1994–2001.

Hewitt, E. and Hewitt, R. (1979). The Gibbs-Wilbraham Phenomenon: An Episode in Fourier Analysis. *Archive for History of Exact Sciences Berlin* **21**, 129–160.

Homeier, H. and Steinborn, E. (1996). Some properties of the coupling coefficients of real spherical harmonics and their relation to Gaunt coefficients. *Journal of Molecular Structure: THEOCHEM* **368**, 31–37.

Howard, M., Cowell, P., Boucher, J., Broks, P., Mayes, A., Farrant, A. and Roberts, N. (2000). Convergent neuroanatomical and behavioral evidence of an amygdala hypothesis

of autism. *NeuroReport* **11**, 2931–2935.

Hurdal, M. K. and Stephenson, K. (2004). Cortical cartography using the discrete conformal approach of circle packings. *NeuroImage* **23**, S119S128.

Jones, D., Catani, M., Pierpaoli, C., Reeves, S., Shergill, S., O'Sullivan, M., Golesworthy, P., McGuire, P., Horsfield, M., Simmons, A., Williams, S. and Howard, R. (2006). Age effects on diffusion tensor magnetic resonance imaging tractography measures of frontal cortex connections in schizophrenia. *Human Brain Mapping* **27**, 230–238.

Joshi, S. (1998). *Large Deformation Diffeomorphisms and Gaussian Random Fields for Statistical Characterization of Brain Sub-Manifolds*.

Joshi, S., Grenander, U. and Miller, M. (1997). The geometry and shape of brain submanifolds. *International Journal of Pattern Recognition and Artificial Intelligence: Special Issue on Processing of MR Images of the Human* **11**, 1317–1343.

Joshi, S., Pizer, S., Fletcher, P., Yushkevich, P., Thall, A. and Marron, J. (2002). Multiscale deformable model segmentation and statistical shape analysis using medial descriptions. *IEEE Transactions on Medical Imaging* **21**, 538–550.

Kelemen, A., Szekely, G. and Gerig, G. (1999). Elastic model-based segmentation of 3-d neuroradiological data sets. *IEEE Transactions on Medical Imaging* **18**, 828–839.

Lazar, M., Weinstein, D., Tsuruda, J., Hasan, K., Arfanakis, K., Meyerand, M., Badie, B., Rowley, H., Haughton, V., Field, A., Witwer, B. and Alexander, A. (2003). White matter tractography using tensor deflection. *Human Brain Mapping* **18**, 306–321.

Lerch, J. P. and Evans, A. (2005). Cortical thickness analysis examined through power analysis and a population simulation. *NeuroImage* **24**, 163–173.

Leventon, M., Grimson, W. and Faugeras, O. (2000). Statistical shape influence in geodesic active contours. In *IEEE Conference on Computer Vision and Pattern Recognition*, volume 1.

Lord, C., Rutter, M. and Couteur, A. (1994). Autism diagnostic interviewrevised: a revised version of a diagnostic interview for caregivers of individuals with possible pervasive developmental disorders. *J Autism Dev Disord.* pages 659–685.

Lorensen, W. and Cline, H. (1987). Marching cubes: A high resolution 3D surface construction algorithm. In *Proceedings of the 14th annual conference on Computer graphics and interactive techniques*, pages 163–169.

Luders, E., Thompson, P.M., Narr, K., Toga, A., Jancke, L. and Gaser, C. (2006). A

curvature-based approach to estimate local gyrification on the cortical surface. *NeuroImage* **29**, 1224–1230.

Lundqvist, D., Flykt, A. and Ohman, A. (1998). *Karolinska Directed Emotional Faces*. Department of Neurosciences, Karolinska Hospital, Stockholm, Sweden.

MacDonald, J., Kabani, N., Avis, D. and Evans, A. (2000). Automated 3-D extraction of inner and outer surfaces of cerebral cortex from mri. *NeuroImage* **12**, 340–356.

Mai, J., Assheuer, J. and Paxinos, G. (1997). *Atlas of the Human Brain*. Academic Press, San Diego.

Miller, M., Banerjee, A., Christensen, G., Joshi, S., Khaneja, N., Grenander, U. and Matejic, L. (1997). Statistical methods in computational anatomy. *Statistical Methods in Medical Research* **6**, 267–299.

Miller, M., Massie, A., Ratnanather, J., Botteron, K. and Csernansky, J. (2000). Bayesian construction of geometrically based cortical thickness metrics. *NeuroImage* **12**, 676–687.

Nacewicz, B., Dalton, K., Johnstone, T., Long, M., McAuliff, E., Oakes, T., Alexander, A. and Davidson, R. (2006). Amygdala volume and nonverbal social impairment in adolescent and adult males with autism. *Arch. Gen. Psychiatry* **63**, 1417–1428.

Nain, D., Styner, M., Niethammer, M., Levitt, J., Shenton, M., Gerig, G., Bobick, A. and Tannenbaum, A. (2007). Statistical shape analysis of brain structures using spherical wavelets. In *IEEE Symposium on Biomedical Imaging ISBI*.

Pierce, K., Muller, R.A., A. J., Allen, G. and Courchesne, E. (2001). Face processing occurs outside the fusiform "face area" in autism: evidence from functional mri. *Brain* **124**, 2059–2073.

Pizer, S., Fritsch, D., Yushkevich, P., Johnson, V. and Chaney, E. (1999). Segmentation, registration, and measurement of shape variation via image object shape. *IEEE Transactions on Medical Imaging* **18**, 851–865.

Qiu, A., and Miller, M. (2008). Multi-structure network shape analysis via normal surface momentum maps. *NeuroImage* **42**, 1430–1438.

Rojas, D., Smith, J., Benkers, T., Camou, S., Reite, M. and Rogers, S. (2000). Hippocampus and amygdala volumes in paretns of children with autistic disorder. *The Canadian Journal of Statistics* **28**, 225–240.

Roy, S. (1953). On a heuristic method of test construction and its use in multivariate analysis. *Ann. Math. Statist.* **24**, 220–238.

Saad, Z., Reynolds, R., Argall, B., Japee, S. and Cox, R. (2004). Suma: an interface for surface-based intra-and inter-subject analysis with afni. In *IEEE International Symposium on Biomedical Imaging (ISBI)*, pages 1510–1513.

Schumann, C., Hamstra, J., Goodlin-Jones, B., Lotspeich, L., Kwon, H., Buonocore, M., Lammers, C., Reiss, A. and Amaral, D. (2004). The amygdala is enlarged in children but not adolescents with autism; the hippocampus is enlarged at all ages. *Journal of Neuroscience* **24**, 6392–6401.

Shen, L. and Chung, M. (2006). Large-scale modeling of parametric surfaces using spherical harmonics. In *Third International Symposium on 3D Data Processing, Visualization and Transmission (3DPVT)*.

Shen, L., Ford, J., Makedon, F. and Saykin, A. (2004). surface-based approach for classification of 3d neuroanatomical structures. *Intelligent Data Analysis* **8**, 519–542.

Sparks, B., Friedman, S., Shaw, D., Aylward, E., Echelard, D., Artru, A., Maravilla, K., Giedd, J., Munson, J., Dawson, G. and Dager, S. (2002). Brain structural abnormalities in young children with autism spectrum disorder. *Neurology* **59**, 184–192.

Styner, M., Gerig, G., Joshi, S. and Pizer, S. (2003). Automatic and robust computation of 3d medial models incorporating object variability. *International Journal of Computer Vision* **55**, 107–122.

Taylor, J. and Worsley, K. (2008). Random fields of multivariate test statistics, with applications to shape analysis. *Annals of Statistics* page in press.

Thompson, P., Giedd, J., Woods, R., MacDonald, D., Evans, A. and Toga, A. (2000). Growth patterns in the developing human brain detected using continuum-mechanical tensor mapping. *Nature* **404**, 190–193.

Thompson, P. and Toga, A. (1996). A surface-based technique for warping 3-dimensional images of the brain. *IEEE Transactions on Medical Imaging* **15**.

Thompson, P. M., MacDonald, D., Mega, M. S., Holmes, C. J., Evans, A. C. and Toga, A. W. (1997). Detection and mapping of abnormal brain structure with a probabilistic atlas of cortical surfaces. *J. Comput. Assist. Tomogr.* **21**, 567–581.

Timsari, B. and Leahy, R. (2000). An optimization method for creating semi-isometric flat maps of the cerebral cortex. In *The Proceedings of SPIE, Medical Imaging*.

Weyl, H. (1910). ÜBer die gibbs sche erscheinung und verwandte konvergenzphÄnomene. *Rendiconti del Circolo Matematico di Palermo* **30**, 377–407.

Wilbraham, H. (1848). On a certain periodic function. *Cambridge and Dublin Math. Journal* **3**, 198–201.

Worsley, K., Marrett, S., Neelin, P., Vandal, A., Friston, K. and Evans, A. (1996). A unified statistical approach for determining significant signals in images of cerebral activation. *Human Brain Mapping* **4**, 58–73.

Worsley, K., Taylor, J., Carbonell, F., Chung, M., Duerden, E., Bernhardt, B., Lyttelton, O., Boucher, M. and Evans, A. (2009). Surfstat: A matlab toolbox for the statistical analysis of univariate and multivariate surface and volumetric data using linear mixed effects models and random field theory. In *International Conference for Human Brain Mapping*, volume 972.

Worsley, K., Taylor, J., Tomaiuolo, F. and Lerch, J. (2004). Unified univariate and multivariate random field theory. *NeuroImage* **23**, S189–195.

Yezzi, A. and Prince, J. (2001). A pde approach for measuring tissue thickness. In *IEEE COMPUTER SOCIETY CONFERENCE ON COMPUTER VISION AND PATTERN RECOGNITION (CVPR)*.

Yu, P., Grant, P., Qi, Y., Han, X., Segonne, F., Pienaar, R., Busa, E., Pacheco, J., Makris, N., Buckner, R. et al. (2007). Cortical Surface Shape Analysis Based on Spherical Wavelets. *IEEE Transactions on Medical Imaging* **26**, 582.

Appendix

We briefly show SurfStat MATLAB command lines to illustrate how the multivariate linear modeling can be done in few statistical models illustrated through the paper. The detailed description of the SurfStat package can be found in `www.stat.uchicago.edu/~worsley/surfstat`. The SurfStat is a general purpose surface analysis package and it requires additional codes for amygdala specific analysis. Additional codes for amygdala shape analysis are available at
`www.stat.wisc.edu/~mchung/research/amygdala`.

Given an amygdala mesh `surf`, which is, for instance, given as a structured array of the form

```
surf =
    vertices: [1270x3 double]
```

```
      faces: [2536x3 double]
```

The amygdala flattening algorithm will generate the corresponding unit sphere mesh `sphere` that has identical topology as `surf`. The weighted spherical harmonic representation `P` with degree $k = 42$ and the bandwidth $\sigma = 0.001$ is computed by running

```
>[P,coeff]=SPHARMsmooth(surf,sphere,42,0.001);
```

The detailed step-by-step MATLAB command line instructions are given in the website. The package also contains few modification of SurfStat for amygdala specific data manipulation and visualization.

The coordinates of the weighted spherical harmonic representation has been read into an array of size 46 (subjects) $\times$ 2562 (vertices) $\times$ 3 (coordinates) `P`. Brain size `brain`, age `age`, group variable `group` and other covariates are read into 46 (subjects) $\times$ 1 vectors. The group categorical variable consists of strings `'control'` and `'autism'`. We now convert these to terms that can be combined into a linear model as follows:

```
>Brain = term( brain );
>Age = term( age );
>Group = term ( group );
>Group
autism  control
---------------
  0       1
  0       1
  1       0
  1       0
  .         .
  .         .
  .         .
```

To test the effect of group, the linear model of the from `P = 1 + Group` is fitted by

```
>E = SurfStatLinMod( P,1 + Group, Avg );
```

where `Avg` is the pre-computed average surface obtained from the weighted spherical harmonic representation. To specify a group contrast and calculate the T-statistic:

```
>contrast = Group.autism - Group.control
contrast =
    -1
    -1
     1
     1
     .
     .
     .
LM = SurfStatT( E, contrast );
```

`LM.t` gives the vector of 2562 T-statistic values for all mesh vertices. Instead of using the contrast and T-statistic, we can test the effect of group variable using the F-statistic:

```
>E0 = SurfStatLinMod( P,1 );
>LM = SurfStatF( E,E0 );
```

`E0` contains the information about the sum of squared residual of the reduced model `P = 1` in `E0.SSE` while `E` contains that of the full model `P = 1 + Group`. Based on the ratio of the sum of squared residuals, `SurfStatF` computes the F-statistics. To display the F-statistic value on top of the average surface, we use `FigureOrigami( Avg, LM.t )` (Figure 8).

To determine the random field based thresholding corresponding to $\alpha = 0.1$ level

```
>resels = SurfStatResels(LM);
>stat_threshold( resels, length(LM.t),1,LM.df,0.1,[],[],[],LM.k)
peak_threshold =
   26.9918
```

`resels` computes the resels of the random field and `peak_threshold` is the threshold corresponding to 0.1 level.

We can construct a more complicated model that includes the brain size and age as covariates:

```
>E0 = SurfStatLinMod(P,Age+Brain);
>E = SurfStatLinMod(P,Age+Brain+Group,Avg);
>LM = SurfStatF(E,E0);
```

`LM.t` contains the F-statistic of the significance of group variable while accounting for age and brain size. To test for interaction between gaze fixation `Fixation` and group variable

```
>E0=SurfStatLinMod(P,Age+Brai +Group+Fixation);
>E=SurfStatLinMod(P,Age+Brain+Group+Fixation+Group*Fixation,Avg);
>LM=SurfStatF(E,E0);
```